Revisiting dynamics and models of microsegregation during polycrystalline solidification of binary alloy

Tongzhao Gong, Yun Chen, Shanshan Li, Yanfei Cao, Dianzhong Li, Xing-Qiu Chen, Guillaume Reinhart, Henri Nguyen-Thi

Revisiting dynamics and models of microsegregation during polycrystalline solidification of binary alloy

Tongzhao Gong [a, b], Yun Chen [a *], Shanshan Li [a, b], Yanfei Cao [a], Dianzhong Li [a], Xing-Qiu Chen [a], Guillaume Reinhart [c], Henri Nguyen-Thi [c]

[a] *Shenyang National Laboratory for Materials Science, Institute of Metal Research, Chinese Academy of Sciences, Shenyang 110016, P. R. China*

[b] *School of Materials Science and Engineering, University of Science and Technology of China, Hefei 230026, P. R. China*

[c] *Aix Marseille Univ, Université de Toulon, CNRS, IM2NP, Marseille, France*

Abstract

Microsegregation formed during solidification is of great importance to material properties. The conventional Lever rule and Scheil equation are widely used to predict solute segregation. However, these models always fail to predict the exact solute concentration at a high solid fraction because of theoretical assumptions. Here, the dynamics of microsegregation during polycrystalline solidification of refined Al-Cu alloy is studied via two- and three-dimensional quantitative phase-field simulations. Simulations with different grain refinement level, cooling rate, and solid diffusion coefficient demonstrate that solute segregation at the end of solidification (i.e. when the solid fraction is close to unit) is not strongly correlated to the grain morphology and back diffusion. These independences are in accordance with the Scheil equation which only relates to the solid fraction, but the model predicts a much higher liquid concentration than simulations. Accordingly, based on the quantitative phase-field

[*]Corresponding author. Tel: +86 24 8397 0106; Fax: +86 24 8397 0097.
E-mail address: chenyun@imr.ac.cn (Y. Chen).

simulations, a new analytical microsegregation model is derived. Unlike the Scheil equation or the Lever rule that respectively overestimates or underestimates the liquid concentration, the present model predicts the liquid concentration in a pretty good agreement with phase-field simulations, particularly at the late solidification stage.

Keywords: microsegregation; grain refinement; cooling rate; back diffusion; phase-field method.

1. Introduction

Microsegregation in as-cast alloys caused by solute partition during solidification is a composition variation at the grain scale (or within the grain), which influences the mechanical properties, corrosion resistance of cast products and formation of macrosegregation [1, 2]. Several microsegregation models with different assumptions and simplifications have been proposed to predict solute redistribution and related phenomena during binary alloy solidification (**Table 1**). The Lever rule [3] describes equilibrium solidification with assuming complete solute diffusion in both liquid and solid phases, and the solute concentration in liquid, C_L, is described as

$$C_L = \frac{C_0}{1-(1-k)\,f_S} \tag{1}$$

where C_0 is the nominal composition, k is the solute partition coefficient, and f_S is the solid fraction. The Lever rule is simple to use but is usually inaccurate because solute diffusion in solid (back diffusion) is very slow for most metallic alloys. To take into account the non-equilibrium effects during alloy solidification, the Scheil equation [3] can be employed to predict the solute concentration in liquid, which still assumes complete solute diffusion in liquid, but neglects diffusion in solid. The solute

concentration in liquid is written as follows

$$C_{\mathrm{L}} = C_0 \left(1 - f_{\mathrm{S}}\right)^{k-1} \tag{2}$$

According to Eq. (2) the Scheil equation is not adequate for predicting the solute concentration at the late solidification stage because $C_{\mathrm{L}} \rightarrow \infty$ (for $k < 1$) or $C_{\mathrm{L}} \rightarrow 0$ (for $k > 1$) as $f_{\mathrm{S}} \rightarrow 1$. Moreover, the liquid concentrations predicted by these two simple models are independent of the microstructure details. In order to predict microsegregation more accurately, several models have been developed by considering the back diffusion, the size and morphology of grains, and coarsening [4-12]. The solute concentration in liquid predicted by those models could be reformulated in a generalized formula as follows

$$C_{\mathrm{L}} = C_0 \left[1 - \left(1 - \Phi k\right) f_{\mathrm{S}}\right]^{\frac{k-1}{1-\Phi k}} \tag{3}$$

where Φ is a parameter linking to both the back diffusion and the grain morphology. The expressions of parameter Φ in Eq. (3) of many previously developed microsegregation models are briefly overviewed in **Table 1**. Its value strongly depends on the solid diffusion coefficient (D_{S}), local solidification time (t_{f}), and the characteristic length of grains (λ), which are included into a parameter, $\alpha = 4D_{\mathrm{S}}t_{\mathrm{f}}/\lambda^2$. However, quantitative analysis in both experiments and numerical simulations has indicated that the effect of back diffusion on microsegregation is very weak for most of metallic alloys [4, 13], since the solute diffusion coefficient in solid is usually 3~4 orders of magnitude smaller than that in liquid. Another important issue is that the characteristic length of grains actually varies with the grain morphology, and therefore an accurate prediction using these derived models must access the dynamical evolution of the grain structure.

Table 1. The expressions of parameter Φ in Eq. (3) in different models.

Microsegregation model	Parameter Φ	References
Scheil equation	$\Phi = 0$	[3]
Lever rule	$\Phi = 1$	[3]
Brody-Flemings model	$\Phi = 2\alpha$	[4]
Clyne-Kurz model	$\Phi = 2\alpha[1 - \exp(-1/\alpha)] - \exp[-1/(2\alpha)]$	[5]
Voller model	$\Phi = 2\alpha/[(1 - f_{eut})^2 + 2\alpha]$	[8]
Voller-Beckermann model	$\Phi = 2\alpha^+/[(1 - f_{eut})^2 + 2\alpha^+]$	[9, 10]
Won-Thomas model	$\Phi = 2\alpha^+[1 - \exp(-1/\alpha^+)] - \exp[-1/(2\alpha^+)]$	[11]

Regarding to the effect of grain morphology, it is well known that the solute distribution strongly relies on the solidification microstructure such as the grain size [14, 15] and the secondary dendritic arm spacing (SDAS) [16], which depends on the process conditions (e.g. the growth rate of columnar grains during directional solidification [17] and the cooling rate during equiaxed solidification [18, 19]). Accordingly, the grain refinement is conventionally viewed as a method to reduce solute segregation [20]. However, this correlation is difficult to be verified directly by traditional experimental methods, since it is influenced by many factors such as melt flow, solidification history and diffusion process after solidification, etc. More significantly, measuring the solute distribution within a grain precisely is a real challenge for 3D dendrites with very complicated shape and branching. The traditional experimental characterization of solute concentration on a sectioned surface from a quenched sample is very likely to be not conserved since the solute transport occurs in

3D space during solidification. The obtained solute concentration that varies with solid fraction may mislead our understanding of the actual solute segregation dynamics. The developed numerical simulation techniques, like the cellular automaton (CA) method [21-23] and the phase-field (PF) [24-26] method, have been powerful tools to investigate microstructure evolution during alloy solidification. Recently, 3D PF simulations regarding details of microstructure evolution by Ohno et al. [13] provided a more accurate prediction for microsegregation. However, their PF simulations only focused on a single crystal and thus might not be able to describe the collective segregation behavior in polycrystalline solidification.

In this paper, the multi-grain growth of Al-Cu alloy during isothermal solidification of equiaxed crystals under continuous cooling condition is studied using a quantitative PF method. Effects of grain refinement, cooling rate, and back diffusion on microsegregation are investigated to give a clear picture of the dynamics of solute segregation in alloys during equiaxed solidification. Based on the analysis of the quantitative PF simulations, a new analytical microsegregation model is developed to provide a more accurate prediction for solute concentration, particularly at the late solidification stage with a high solid fraction. The model differs markedly from the Scheil equation and Lever rule, or any of their derivative models, but remains simple and easy-to-use. Consequently, it has great potential to be embedded into macrosegregation models of ingots [27-30] or the CALPHAD (*CALculation of PHAse Diagram*) software packages, such as Thermo-Calc [31], to calculate the stable phase formation during solidification based on the predicted solute concentration with thermodynamic databases.

2. The phase-field model and numerical implementations

2.1 The quantitative PF model of equiaxed dendritic growth of a binary alloy

The quantitative PF model presented in Ref. [32] is adopted to model slow solidification of binary alloys under continuous cooling condition, and the quantitative capability of this model to reproduce the time evolution of microstructure during alloy solidification has been demonstrated in many previous studies [33-36]. The governing equations of the phase field ϕ and the rescaled solute concentration U are respectively given as

$$\left(1+\frac{R_c t}{|m|C_0}\right)\tau(\mathbf{n})\frac{\partial\phi}{\partial t}=\nabla\cdot\left[W(\mathbf{n})^2\nabla\phi\right]+\sum_{i=x,y,z}\partial_i\left[|\nabla\phi|^2 W(\mathbf{n})\frac{\partial W(\mathbf{n})}{\partial(\partial_i\phi)}\right] +\phi-\phi^3-\lambda\left[U-\frac{R_c t}{(1-k)|m|C_0}\right]\left(1-\phi^2\right)^2 \tag{4}$$

$$\frac{(1+k)-(1-k)\phi}{2}\frac{\partial U}{\partial t}=\nabla\cdot\left\{D\frac{1-\phi}{2}\nabla U+\frac{W_0\left[1+(1-k)U\right]}{2\sqrt{2}}\frac{\partial\phi}{\partial t}\frac{\nabla\phi}{|\nabla\phi|}\right\} +\frac{1+(1-k)U}{2}\frac{\partial\phi}{\partial t} \tag{5}$$

with

$$U=\frac{2C/C_0-\left[(1+k)-(1-k)\phi\right]}{(1-k)\left[(1+k)-(1-k)\phi\right]} \tag{6}$$

where C is the local solute concentration, C_0 is the initial concentration, k is the solute partition coefficient, R_c is the cooling rate, and m is the liquidus slope. The solid and liquid phases are represented by $\phi = +1$ and $\phi = -1$, respectively. The spatial length and time are rescaled respectively by the interface width W_0 and relaxation time τ_0, and therefore the dimensionless value for the solute diffusion coefficient in liquid is

$$\tilde{D}=\frac{D\tau_0}{W_0^2}=a_1 a_2\frac{W_0}{d_0} \tag{7}$$

where $d_0 = \Gamma/[|m|C_0(1-k)]$ is the chemical capillary length with Γ the Gibbs-Thomson coefficient, $a_1 = 5\sqrt{2}/8$ and $a_2 = 47/75$ [32]. The coupling coefficient λ in Eq. (4) is

given as $\lambda = a_1 W_0/d_0$. The standard form of the fourfold symmetry of the surface energy anisotropy is considered, and thus $W(\mathbf{n}) = W_0 a_s(\mathbf{n})$ and $\tau(\mathbf{n}) = \tau_0 a_s(\mathbf{n})^2$ where

$$a_s(\mathbf{n}) = 1 - 3\varepsilon_4 + 4\varepsilon_4 \sum_{i=x,y,z} \frac{(\partial_i \phi)^4}{|\nabla \phi|^4} \tag{8}$$

In order to expedite large-scale quantitative PF simulations, a nonlinear preconditioning [37] of the phase field ϕ is employed to allow coarser grids to be used in the interface layer. The transformed phase field ψ is given as

$$\psi = \tanh\left(\frac{\phi}{\sqrt{2}}\right) \tag{9}$$

And hence the standard PF model (Eqs. (4) and (5)) is transformed into the nonlinearly preconditioned formula, as follows

$$\begin{aligned}\left(1 + \frac{R_c t}{|m| C_0}\right)\tau_0 a_s^2(\mathbf{n})\frac{\partial \psi}{\partial t} &= W_0^2 a_s^2(\mathbf{n})\left[\nabla^2\psi - \sqrt{2}\tanh\left(\frac{\psi}{\sqrt{2}}\right)|\nabla\psi|^2\right] \\ &+ \sum_{i=x,y,z} W_0^2 \partial_i\left[|\nabla\psi|^2 a_s(\mathbf{n})\frac{\partial a_s(\mathbf{n})}{\partial(\partial_i\psi)}\right] + \sqrt{2}\tanh\left(\frac{\psi}{\sqrt{2}}\right) \\ &- \sqrt{2}\lambda\left[1 - \tanh^2\left(\frac{\psi}{\sqrt{2}}\right)\right]\left[U - \frac{R_c t}{(1-k)|m| C_0}\right]\end{aligned} \tag{10}$$

$$\begin{aligned}&\frac{(1+k) - (1-k)\tanh\left(\frac{\psi}{\sqrt{2}}\right)}{2}\frac{\partial U}{\partial t} \\ &= \nabla\cdot\left\{D\frac{1 - \tanh\left(\frac{\psi}{\sqrt{2}}\right)}{2}\nabla U + \frac{1}{2}W_0\left[1 + (1-k)U\right]\frac{1 - \tanh^2\left(\frac{\psi}{\sqrt{2}}\right)}{2}\frac{\partial\psi}{\partial t}\frac{\nabla\psi}{|\nabla\psi|}\right\} \\ &+ \frac{1 + (1-k)U}{2}\frac{1 - \tanh^2\left(\frac{\psi}{\sqrt{2}}\right)}{\sqrt{2}}\frac{\partial\psi}{\partial t}\end{aligned} \tag{11}$$

The numerical accuracy and efficiency of the preconditioned PF formula has been examined carefully [38]. The detailed numerical and material parameters can be referred to our previous study [39], but C_0 is set to be 1 wt.% to result in a larger

capillary length. Large-scale simulations can be therefore realized quantitatively in a relatively wide range of cooling rates. The interface width parameter, $\xi = W_0/d_0$, is determined according to the convergence tests (**Fig. S1** in the supplementary materials) to guarantee the results of simulations being quantitative.

2.2 The numerical implementations

The parallel adaptive finite element method, with multiple processors using distributed memory based on the MPI protocol, is employed to solve the nonlinearly preconditioned PF model. Numerical implementations are realized by the open source deal.II library [40], and the adaptive mesh refinement/coarsening is achieved through a simple but efficient approach [38]. The front-tracking method [38] is used to capture crystallographic orientations to improve the computing efficiency dramatically. The computational domain size is 5×5 mm^2 and $1 \times 1 \times 1$ mm^3, respectively in 2D and 3D simulations. Grains nucleate simultaneously at the beginning of simulations, with the number of grains 36~324 in the 2D simulations and 8~125 in the much more time-consuming 3D simulations. All the simulations were carried out on a supercomputer with an Intel® Xeon E5-2683 v4 CPU (2.10 GHz and 32 cores) and 256 GB memory at each computing node. For the 2D simulation with the lowest cooling rate (0.01 K/s) and the largest grain number (324), it took about 14 days using 96 cores to finish the computation until the solid fraction $f_S = 0.99$, and most of the regions which were not solidified formed grain boundaries eventually. Here, totally solidified zones are defined as $\psi \geq 0$. However, the 3D simulations were ended at a relatively low solid fraction ($f_S = 0.25$) because of the unbearable computing time when grains impinged.

3. Dynamic evolution of microsegregation in polycrystalline alloy

3.1 Effects of the grain refinement on the solute segregation

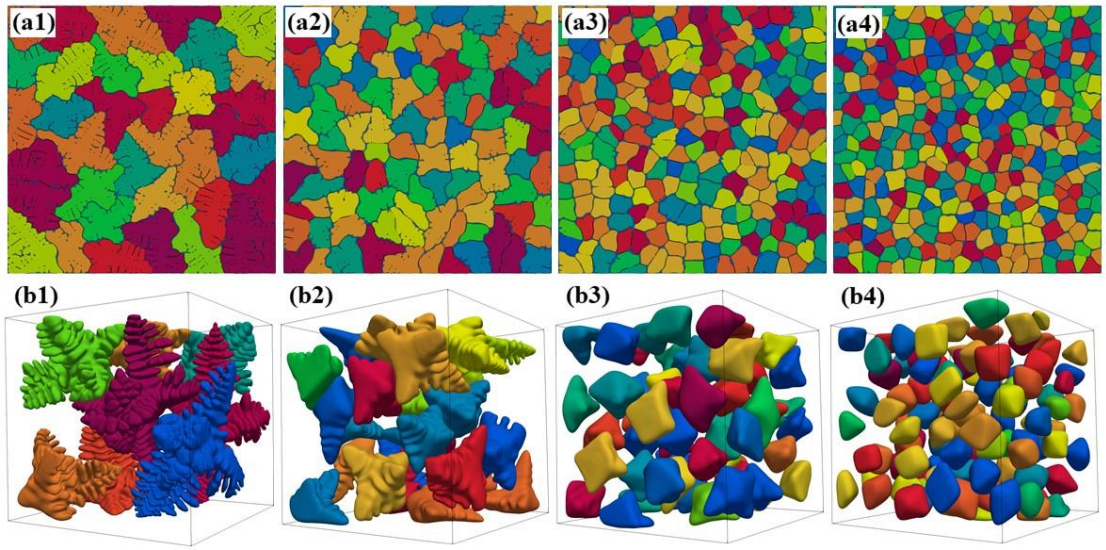

Fig. 1. Equiaxed dendritic microstructure of Al-1 wt.% Cu alloy at a cooling rate R_c = 0.1 K/s with different grain numbers, N, respectively at solid fraction f_S = 0.9 in the 2D (**a1** to **a4**) and f_S = 0.2 in 3D (**b1** to **b4**) PF simulations. (**a1**) N = 36; (**a2**) N = 100; (**a3**) N = 225; (**a4**) N = 324; (**b1**) N = 8; (**b2**) N = 27; (**b3**) N = 64; (**b4**) N = 125. The colors represent the crystal orientations.

The equiaxed dendritic microstructure of refined Al-1 wt.% Cu alloy during isothermal solidification with a constant cooling rate R_c = 0.1 K/s in the 2D and 3D PF simulations is shown in **Fig. 1** for various imposed number of grains. As the number of grains increases (by artificially adding more nucleation sites in simulations), the grain size becomes smaller and smaller, and the equiaxed crystal shape evolves from highly branched dendrite to nearly uniform globular, with the secondary arms less developed and even disappearing. Changes in the grain size and morphology can be attributed to the solute interaction between neighboring grains, which suppresses the growth of primary arms and the development of sidebranches, therefore bringing out a much denser equiaxed dendritic microstructure. The solute interaction between grains has

been well characterized through the in situ and real-time observation of Al-Cu solidification experiments performed by Bogno et al. [41]. They have found that equiaxed dendritic growth experiences two regimes, namely the free growth and the impinged growth. Impingement causes grain growth being slowed down or even stopped. The impinged growth took most of the computing time to complete solidification in current simulations, particularly for 3D computations.

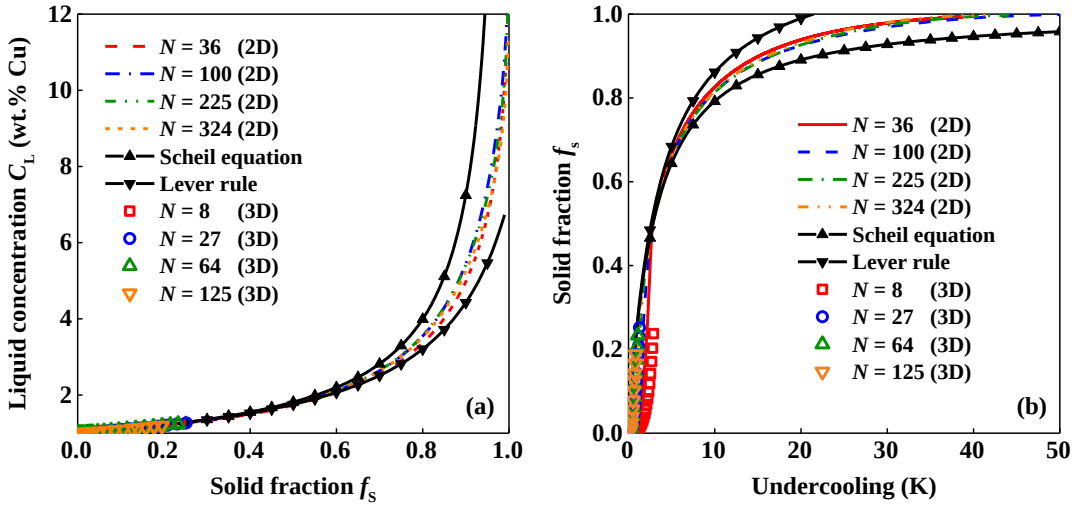

Fig. 2. The average solute concentration in liquid, C_L (**a**), and the solid fraction, f_S (**b**), in the 2D and 3D PF simulations of Al-1 wt.% Cu alloy at R_c = 0.1 K/s with different grain numbers. The predictions by the Scheil equation and Lever rule are also plotted.

The average liquid concentration, C_L, in both 2D and 3D simulations is plotted in **Fig. 2**(a). In general, the simulated C_L in both 2D and 3D with different number of grains almost fall in one curve. Apart from a slight difference that branched dendrites will cause a slightly lower C_L, the evolution of C_L shows no strong dependence on the grain morphology, for either dendrites with developed branches or nearly globular grains with smooth interface. Furthermore, C_L in the PF simulations, as expected, falls in between the predictions by the Scheil equation and Lever rule. At the early

solidification stage (f_S < 0.55) both analytical models predict C_L identical to the simulations, indicating that the grain morphology is not a crucial factor to affect C_L at a low solid fraction. As solidification proceeds, the grain impingement takes place (characterized by the slow-down increasing rate of f_S in **Fig. 2**(b) at t ~ 30 s) and the analytical predictions deviate gradually from the PF simulations.

Fig. 2(b) shows the variation of solid fraction as a function of undercooling. Like the average solute concentration in liquid, the solid fraction has no significant correlation to the number of grains (or the grain morphology) too, and f_S in the PF simulations is close to the predictions by the Scheil equation and Lever rule as f_S < 0.55. However, as f_S increases furtherly, it evolves gradually in between the predictions by these two microsegregation models. It is worthy noticing that, no visible difference in C_L can be found here between 2D and 3D simulations (**Fig. 2** (a)). Even though it has been quantitatively convinced that the crystal growth kinetics and solute transport are different in 2D and 3D PF simulations [42], the difference in solute transport in 2D planar and 3D cubic space could be offset because solute is rejected from solid into liquid through a curve in 2D while a surface in 3D. Unlike the traditional experimental measurement of solute distribution on a sectioned 2D surface where the conservation of measured solute cannot be ensured, the 2D simulations here like the 3D simulation always guarantee the solute conservation during the entire solidification process, and are therefore feasible to reveal the dynamic evolution of microsegregation.

Prediction for C_L only gives the average solute concentration in the rest of liquid but does not describe the spatial distribution of solute. The segregation extent can be quantitatively evaluated using the solute segregation index, $S_I = \frac{1}{V}\int_V \frac{|C_i - C_0|}{C_0} dV$ with C_i the solute concentration at the ith quadrature point (in both solid and liquid

phases in the computational domain of PF simulations) and V the total domain volume. S_I should be more appropriate to evaluate the segregation extent than the mean solid or liquid solute concentration, as S_I spatially measures the deviation of the solute concentration from C_0. The results in 2D and 3D PF simulations are plotted in **Fig. 3**(a). Again, no apparent difference can be found for S_I between 2D and 3D simulations. During the early solidification stage, an increasing amount of solute is rejected into liquid and piles up ahead of the solid-liquid interface, thus leading to an increment in S_I. As solidification proceeds, the difference from C_0 for C_L is larger and larger, while for the average solute concentration in solid, C_S, becomes smaller and smaller. As a result, S_I increases to a peak value at $f_S \sim 0.8$, and then drops down with $f_S \rightarrow 1$ because the area of solid weights more and more in the S_I calculation. When f_S is close to 1, though C_L departs from C_0 very obviously (**Fig. 2**(a)), the liquid fraction is so small that the solute distribution in solid plays a dominant role in determining S_I. At the late solidification stage, the solute interaction between grains is going to suppress the growth of crystals, but C_L continues increasing, which could be attributed to the fact that the crystal growth does not stop entirely when the solid fraction is high and the diffusion time is sufficient to homogenize the composition in the sample. The variation trend of S_I observed in **Fig. 3**(a) is independent of the grain number or morphology, but the peak value of S_I is apparently affected by the grain refinement. Interestingly, less grains with developed branches lead to a lower peak value of segregation index, which is consistent with the experimental study of He et al. [16] who have indicated that the decreases in SDAS would reduce the microsegregation. However, values of S_I for different number of grains almost overlap as $f_S \rightarrow 1$ (**Fig. 3**(a)). Again, it is revealed that the segregation extent after complete solidification has no strong correlation to the grain refinement.

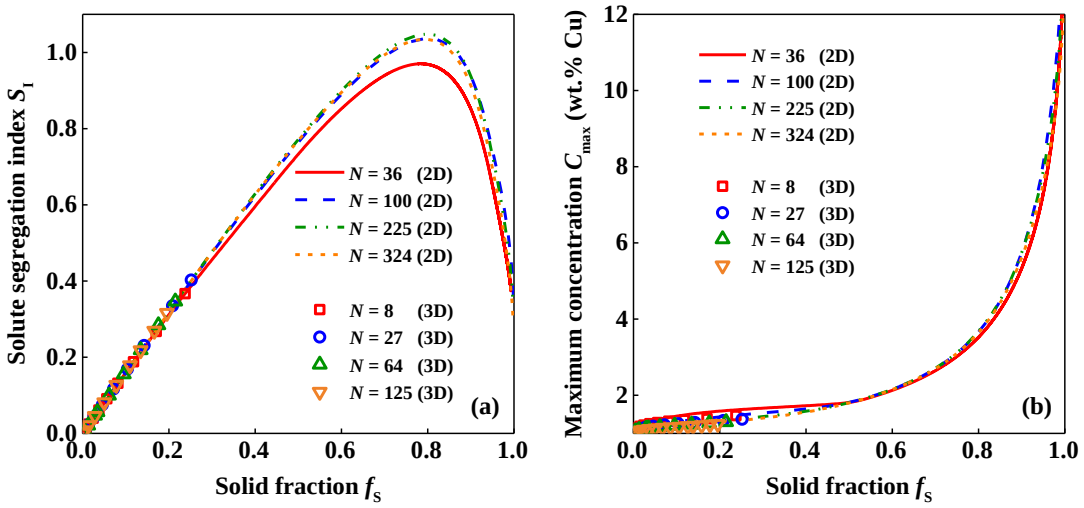

Fig. 3. Variation of S_I (**a**) and C_{max} (**b**) with f_S in the 2D and 3D PF simulations of Al-1 wt.% Cu alloy at R_c = 0.1 K/s. The 3D simulations are ended at a relatively low solid fraction because of the unbearable computing time when grains impinge.

Another parameter quantifying the segregation is the maximum solute concentration in liquid, C_{max} (**Fig. 3**(b)). For interdendritic segregation, C_{max} locates at the root of dendritic branches and can be approximated by the liquidus equilibrium concentration in the phase diagram, $C_L^E = C_0 - \Delta T/m$ with ΔT the applied undercooling. Owing to the curvature effect of the concave solid-liquid interface, C_{max} is in fact slightly larger than the equilibrium concentration C_L^E obtained from the phase diagram. However, this difference is invisible in PF simulations as shown by **Fig. 4**(a to d) and the approximation $C_{max} \approx C_L^E$ sounds reasonable. Another issue is that the grain shape should lead to a slight difference in C_{max}, owing to the different C_L^E arising from the different undercooling required to approach the same solid fraction (**Fig. 2**(b)).

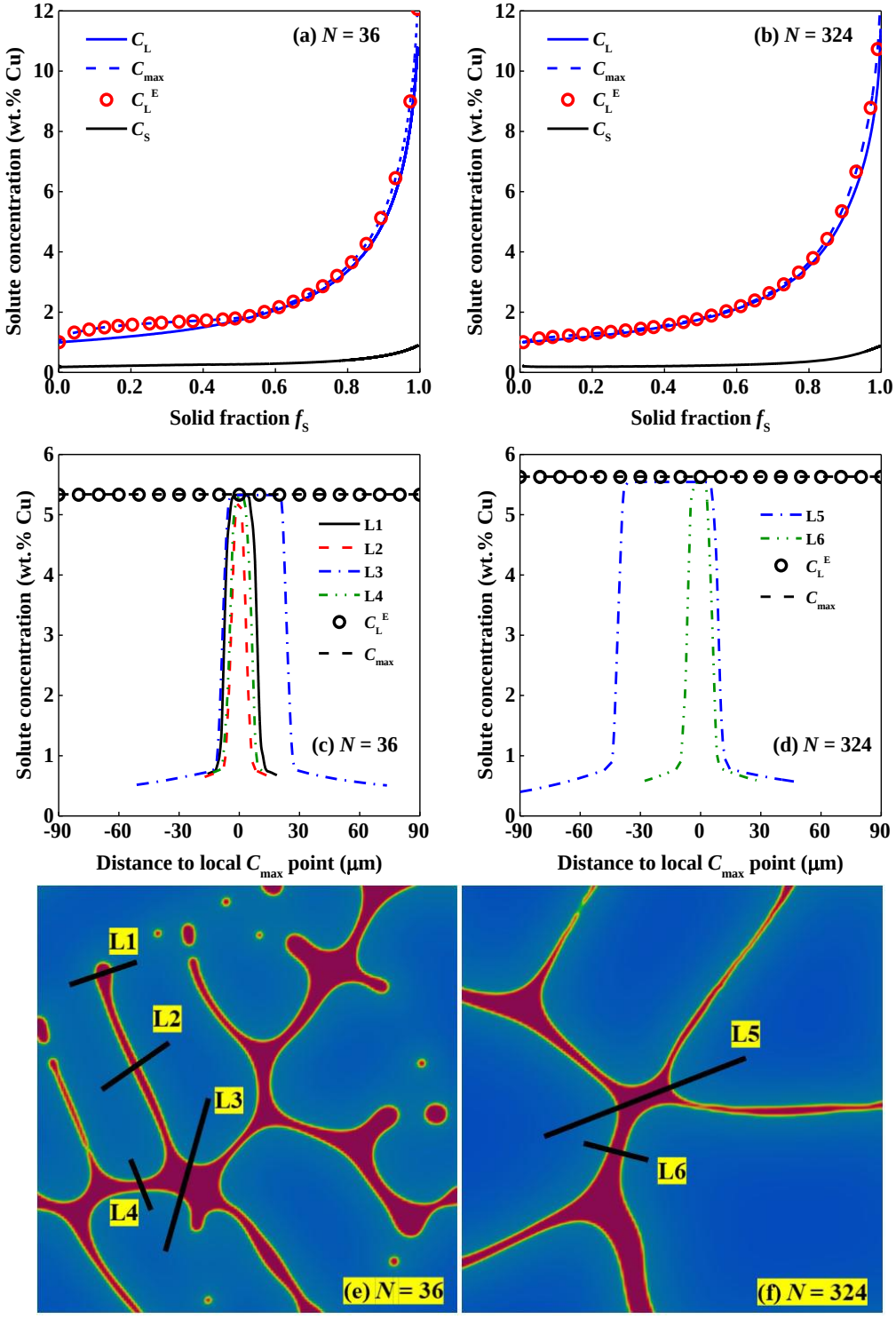

Fig. 4. Solute distribution in the 2D PF simulations of Al-1 wt.% Cu alloy at R_c = 0.1 K/s with N = 36 and 324. (**a** and **b**) Variation of C_L, C_S, C_{max}, and C_L^E against f_S; (**c** and **b**) The solute profile along the lines shown in (e and f) at f_S = 0.9. (**e** and **f**) show the corresponding local grain morphology in the simulations with N = 36 and 324, respectively. Blue is solid and red is residual liquid.

Nevertheless, the apparent enlargement of C_{max} for $N = 36$ in the 2D PF simulation at a low solid fraction ($f_S < 0.5$) is due to the higher undercooling (or solidification time) to reach the same f_S (**Fig. 2**(b)). It means that liquid is solidified at a higher undercooling for the same solid fraction when grain number is reduced, thereby gaining a higher equilibrium concentration and thus a larger C_{max}. However, as $f_S > 0.5$, C_{max} for $N = 36$ evolves into a slightly lower value than other cases owing to a shorter time taken to get the same f_S (**Fig. 2**(b)). The slight difference in C_{max} with various grain numbers can be seen more apparently in **Fig. 4**(c to f). At the same solid fraction ($f_S = 0.9$), because of the lower undercooling for $N = 36$ (**Fig. 2**(b)), the solute concentration near the interface exhibits a smaller value than that for $N = 324$. To sum up, when the grain number is smaller ($N = 36$), the melt solidifies slower at a low solid fraction ($f_S < 0.5$). In contrast, at the late solidification stage smaller number of grains solidifies a little faster because grains impinge with each other not so terribly as that for high numbers of grains, thus leading to a relatively lower C_L^E and C_{max}, as well as smaller S_I. Obviously, curves of C_L with f_S is always below C_L^E in **Fig. 4**(a and b).

3.2 Effects of the cooling rate on the solute segregation

Rapid solidification has been always considered as an efficient method to reduce segregation. Increasing the cooling rate not only shortens the solute transport time but also refines grains. To clarify the effect of cooling rate on microsegregation, here the solidification of Al-1 wt.% Cu alloy with different cooling rates are simulated and the results are shown in **Fig. 5**. Please notice that with a large cooling rate (e. g. ~1.0 K/s) the quantitative results in the present 2D PF simulations are not able to be ensured even though W_0 has been reduced to 0.4 μm, in which the computational domain size and computing time will be augmented dramatically, making the large-scale quantitative PF

simulations extremely difficult. Therefore, the maximum cooling rate in our PF simulation is limited to R_c = 0.2 K/s, at which the results can still be converged with the given available W_0. Based on the limited range of R_c, the following discussions about the effects of cooling rates on microsegregation are restricted to the slow solidification regime where the local equilibrium at the solid-liquid interface is satisfied. **Fig. 5** shows that when grain number is small (N = 36), a higher cooling rate causes a slightly lower C_L, whereas an opposite behavior is observed when grain number is large (N = 324). These opposite effects should be ascribed to the difference in grain morphology. For N = 36 (**Fig. 5**(g)), as the cooling rate increases the sidebranches have been well developed and SDAS is shortened. For N = 324 (**Fig. 5**(h)), the cooling rate has no obvious effect on grain morphology due to the grain impingement occurs very early, and the longer diffusion time at a lower cooling rate will thereby lead to a better solute homogenization in liquid. Regardless of the cooling rate or grain refinement, it can be drawn that higher undercooling required to reach the same f_S results in higher C_L (**Fig. 4**(c, d) and **Fig. 5**(a, b, e, and f)). However, the effect of cooling rate on C_L is not apparent overall in all these cases and they all evolve along close curves that fall in between the predictions by the Scheil equation and Lever rule.

The effect of cooling rate on the dynamics evolution of C_{max} and S_I is shown in **Fig. 6**. Increasing the cooling rate results in slightly larger C_{max} when f_S < 0.55 (**Fig. 6**(a, b)). This variation is in agreement with the fact that C_{max} strongly depends on the undercooling of the melt so that it varies in the same manner as undercooling shown in **Fig. 5**(e, f). For f_S > 0.55, no significant difference can be found except for the case with N = 324 and R_c = 0.01 K/s, which may be attributed to the well mixing solute in the liquid arising from the narrow spacing between grains and sufficient diffusion time. As the cooling rate increases, S_I is reduced in the simulation with a small grain number

(N = 36 in **Fig. 6**(c)). Lower cooling rate causes a higher peak value of S_I due to the increase in C_L (**Fig. 5**(a)) and SDAS [16] (**Fig. 5**(g and h)). However, analogous to C_L, the influence of cooling rate on S_I shows an opposite trend for a large grain number (N = 324 in **Fig. 6**(d)) with almost globular crystal shape (**Fig. 5**(h)). S_I at the late solidification stage will be enlarged with the cooling rate increasing for N = 324 (**Fig. 6**(d)) and faster cooling causes a higher peak value.

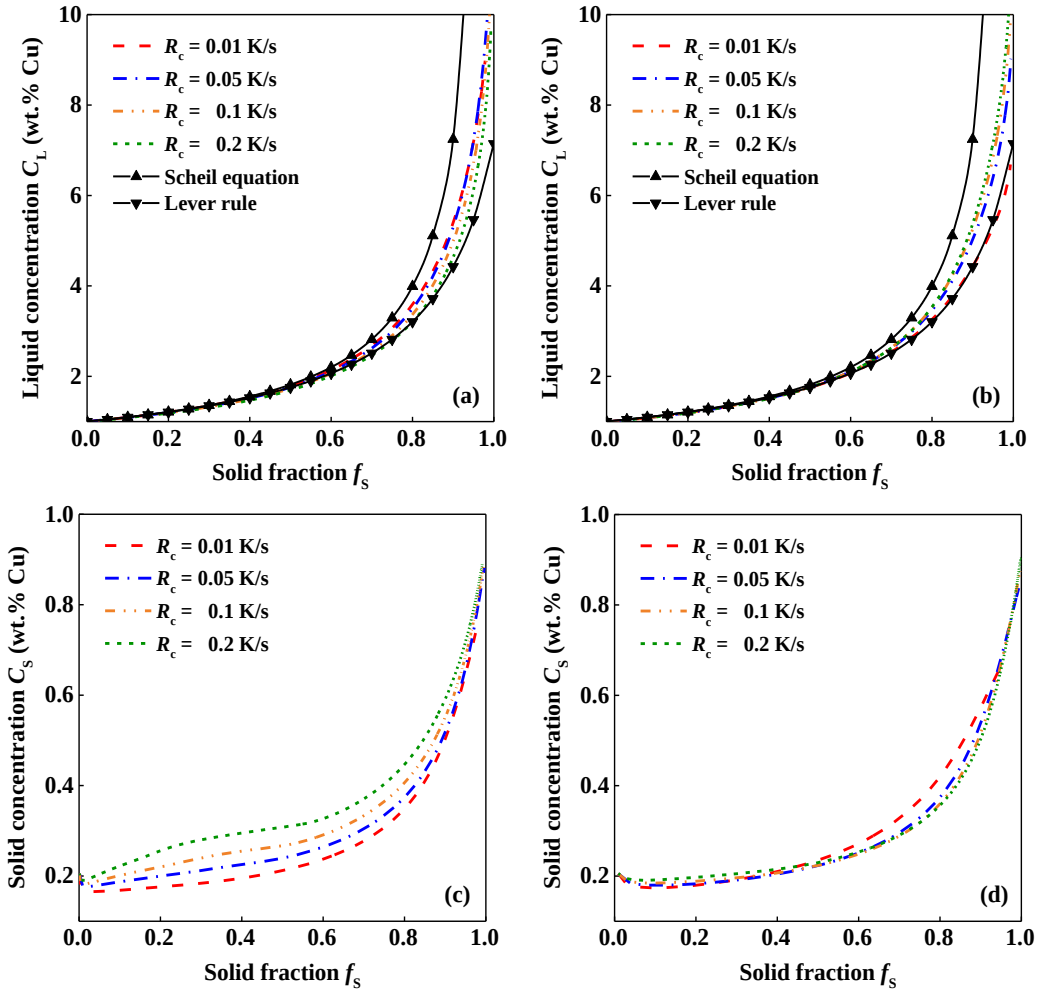

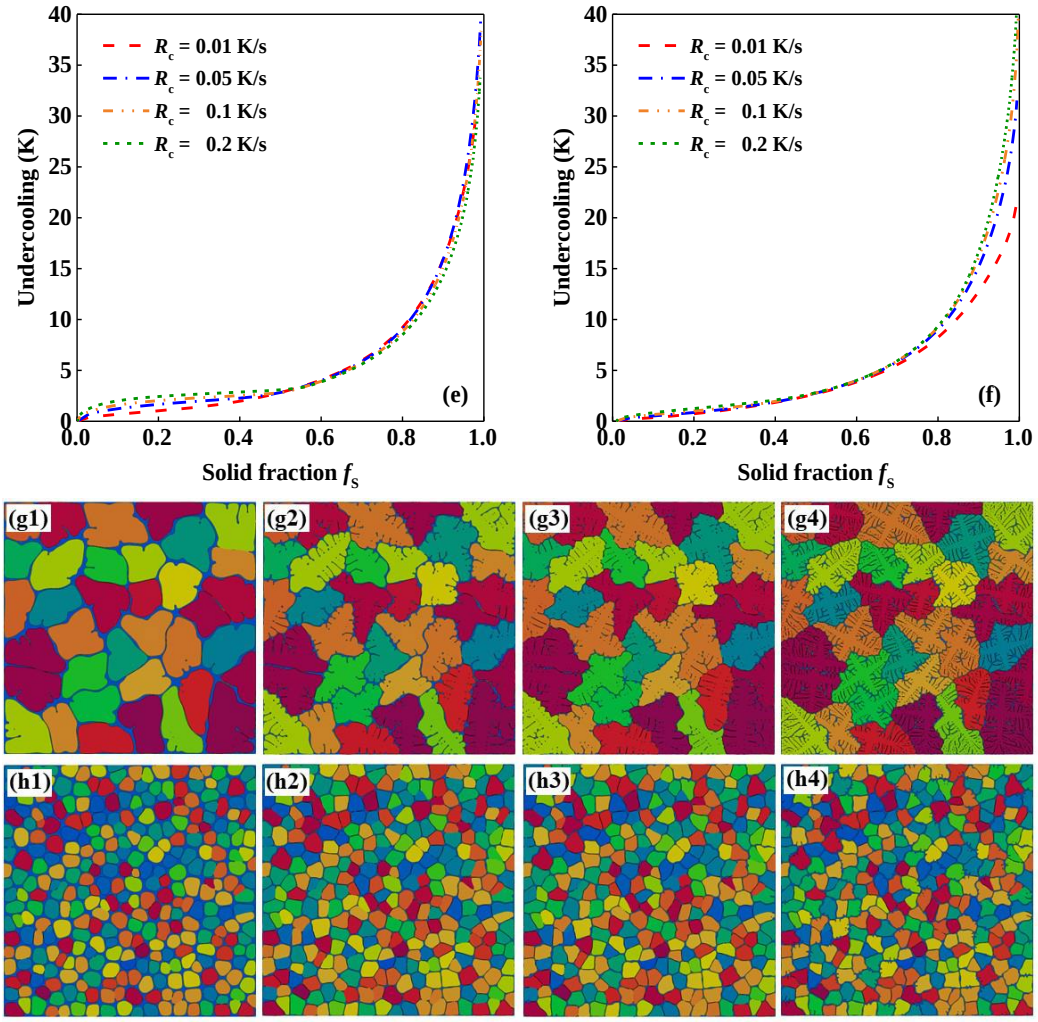

Fig. 5. Effects of the cooling rate on C_L (**a** and **b**), C_S (**c** and **d**), the undercooling (**e** and **f**), and equiaxed dendritic microstructure (**g** and **h**) in the 2D PF simulations of Al-1 wt.% Cu alloy with N = 36 (**a**, **c**, **e**, **g1** to **g4**) and N = 324 (**b**, **d**, **f**, **h1** to **h4**). f_S in (**g** and **h**) is about 0.9, and the colors represent the crystal orientations. The cooling rate is 0.01 K/s (**g1, h1**), 0.05 K/s (**g2, h2**), 0.1 K/s (**g3, h3**) and 0.2 K/s (**g4, h4**).

These different evolution behaviors can be ascribed to that when the grain number is large enough to make the crystal shape almost globular, the sidebranches will not be well developed owing to the strong solute interaction between neighboring grains. In this case, the solute diffusion in liquid plays a dominant role to reduce S_I, and the time for solute homogenization by diffusion at a slower cooling rate is longer, thus leading to a decline in S_I. In contrast, with sufficient space to develop sidebranches, the grain morphology is the main factor affecting the segregation extent. A higher cooling rate

promotes the sidebranch formation, thus leading to a lower S_I arising from smaller C_L and SDAS [16]. Interestingly, similar to the effect of grain number, no matter what extent of the influence by the cooling rate exists during solidification, the curves of S_I eventually drop down to a roughly same value when solidification nearly completes. This is because C_S that occupies most of the computational domain dominates the calculation of S_I at the late solidification stage. As solute should be kept conserved and meet the local equilibrium condition during polycrystalline solidification, C_S approaches to C_0 at the end of solidification for different conditions (**Fig. 5**(c, d)), leading to the coincidence feature of S_I.

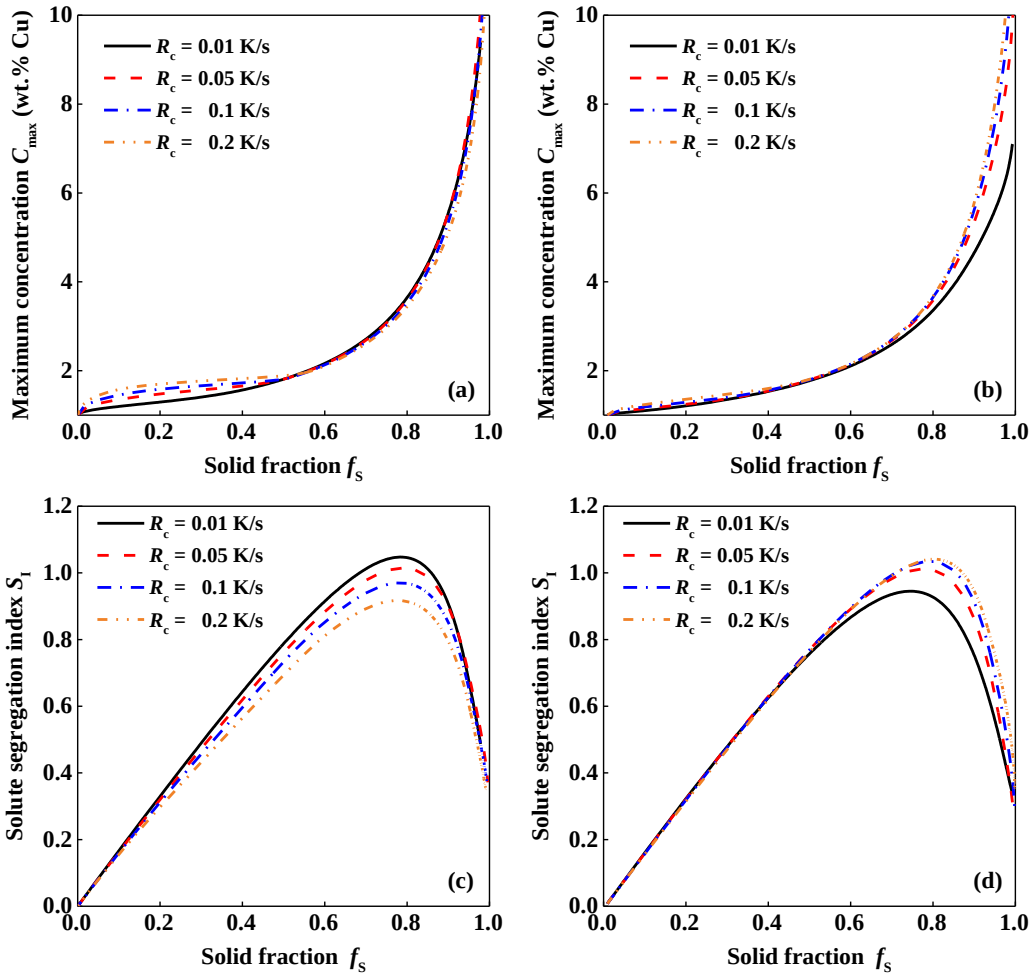

Fig. 6. Effects of cooling rates on the solute segregation behavior in the 2D PF simulations of Al-1 wt.% Cu alloy. C_{max} and S_I at various cooling rates are shown in (**a**, **b**) and (**c**, **d**), respectively. The grain number in (**a**, **c**) is 36, while that in (**b**, **d**) is 324.

3.3 Effects of back diffusion on solute segregation

The back diffusion is commonly considered as an important factor that influences the solute microsegregation behavior. However, for most of metallic alloys, the effect of back diffusion on microsegregation is negligible since the solute diffusion coefficient in solid is usually 3~4 orders of magnitude smaller than that in liquid (e. g. $D_S/D_L \approx 10^{-3}$ for Al-Cu alloys). Here, to ascertain how back diffusion influences microsegregation, the 2D PF simulations at the cooling rate R_c = 0.1 K/s and grain number N = 36 are performed with various solid diffusion coefficients (by artificially changing D_S), and the simulated results including C_L, C_{max}, and S_I are shown in **Fig. 7**. No apparent differences in all these quantities are observed for $f_S < 0.6$. However, as the solid fraction increases furtherly, it will take a relatively shorter time to reach the same f_S with a larger D_S (**Fig. 7**(a)), which causes a lower equilibrium concentration, C_L^E. As C_{max} is equal to C_L^E approximately, C_{max} will also be reduced with a larger D_S (**Fig. 7**(b)), thus leading to a lower average solute concentration, C_L (**Fig. 7**(c)).Therefore, the solute segregation index, S_I, will be lowered as D_S increases (**Fig. 7**(d)).

The microsegregation behavior shown in **Fig. 7** is still consistent with the experimental study by He et al. [16], who have found that decreasing solid diffusion coefficient would give rise to the increase in microsegregation. However, the differences between the curves with no back diffusion ($D_S = 0$) and a small D_S ($10^{-3}D_L$) is not pronounced, which means that the back diffusion is not a crucial factor that influences microsegregation for most of the metallic alloys with a D_S several orders of magnitude smaller than D_L. Furthermore, it is also worth noticing that C_L in the simulation with $D_S/D_L = 10^{-1}$ is very close to the prediction by the Lever rule, which demonstrated that the assumption of complete diffusion in both solid and liquid

employed in the Lever rule is well satisfied with such a large D_S.

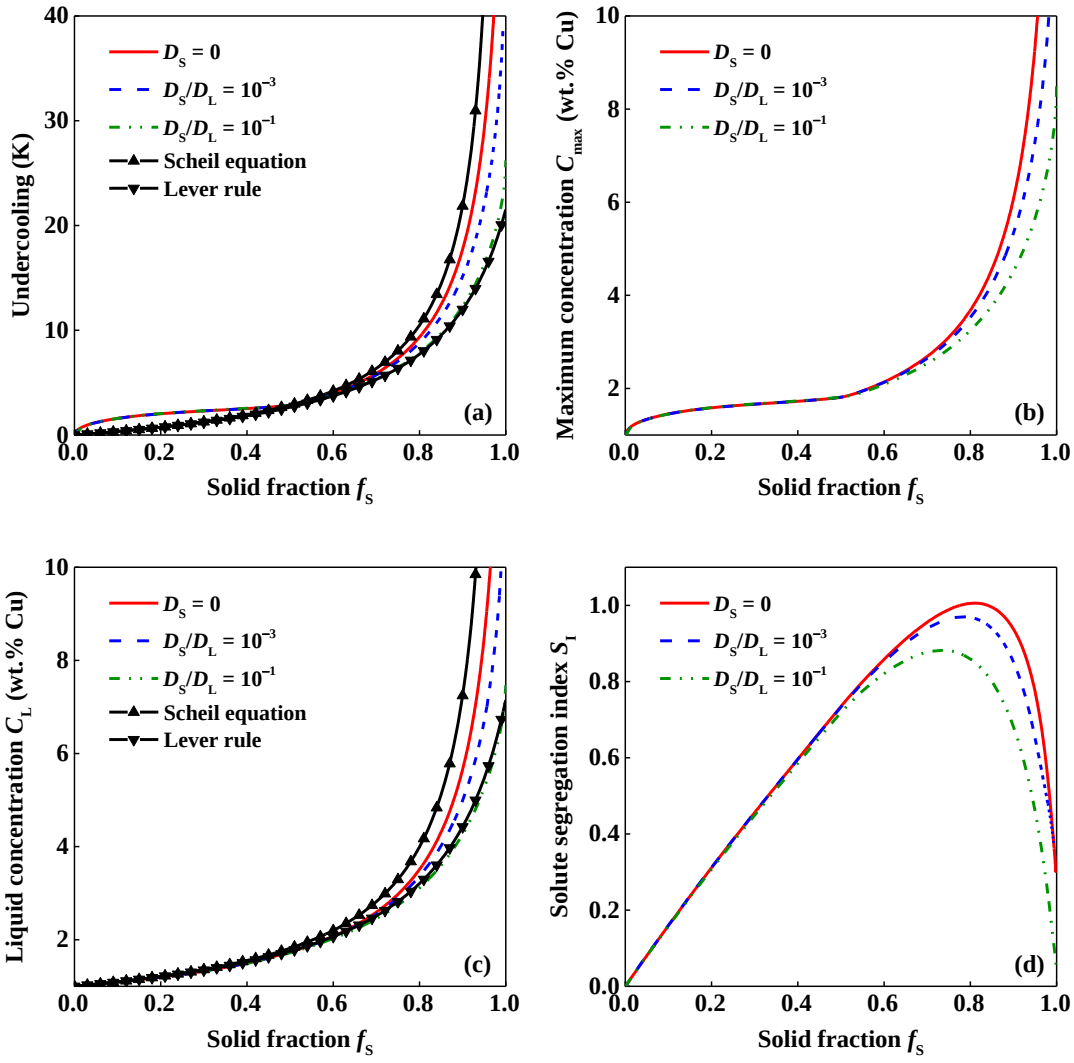

Fig. 7. Variation of the undercooling (**a**), C_{max} (**b**), C_L (**c**), and S_I (**b**) against f_S in the 2D PF simulations of Al-1 wt.% Cu alloy at R_c = 0.1 K/s and N = 36, with various D_S.

4. A new microsegregation model for binary alloys

In terms of above simulations and analysis, it has been confirmed that for relatively slow solidification rather than rapid solidification, the grain morphology, cooling rate, and back diffusion (if not relatively high), have some slight influences on microsegregation but not the crucial factors to change C_L and the final segregation for

substitutional alloys. The liquid concentration in simulations is between the predictions by the Scheil equation and Lever rule, which are two limiting cases for the real non-equilibrium solidification. As already recognized, these two models fail to predict the solute redistribution at the late solidification stage when the solid fraction is close to unit, in particular for Scheil equation which gives a highly unrealistic value ($k < 1$). To overcome this drawback, it is necessary to develop a new model to gain a more accurate prediction for C_L. According to the Lever rule, the solute concentration in liquid during binary alloys solidification is given by Eq. (1). As shown in **Fig. 2**(a), C_L^{Lever} is in a good agreement with the PF simulations at the early solidification stage with $f_S < 0.55$. However, at the late solidification stage as $f_S \to 1$, C_L is much larger than C_L^{Lever} and close to the maximum solute concentration in liquid, C_{max}, owing to that the solute concentration in the very little residual liquid is nearly uniform. It should be noticed that although the Scheil equation describes the limiting case with considering non-equilibrium effects during solidification, the predicted C_L is unrealistic at a high solid fraction, and hence C_{max} is a better choice of the upper limit for C_L. Therefore, C_L could be interpolated between C_L^{Lever} and C_{max} through a function of f_S, as follows

$$C_L = \left[1 - w(f_S)\right] C_L^{Lever} + w(f_S) C_{max} \tag{12}$$

where $w(f_S)$ satisfies

$$\begin{aligned} f_S &= 0,\ w(f_S) = 0 \\ f_S &= 1,\ w(f_S) = 1 \end{aligned} \tag{13}$$

which reflects that C_L changes gradually from the predicted value by the Lever rule (the lower limit) to C_{max} (the upper limit). Even though the geometric shape of the solid-liquid interface leads to C_{max} deviating from C_L^E (the equilibrium liquidus concentration at a given undercooling for a flat interface), C_{max} still could be approximated by C_L^E, as follows

$$C_{\max} \approx C_{\mathrm{L}}^{\mathrm{E}} = C_0 - \frac{\Delta T}{m} \tag{14}$$

with $m < 0$ for $k < 1$. This approximation has been proved by **Fig. 4**(c, d) which shows that $C_{\max}$ at the interdendritic region is very close to $C_{\mathrm{L}}^{\mathrm{E}}$ for both developed dendrites and globular grains. Please notice that $C_{\max}$ is larger than C_0/k when solidification nearly completes because the temperature reached at the end of solidification is lower than the solidus temperature. Eqs. (1) and (14) are substituted into Eq. (12), yielding

$$C_{\mathrm{L}} = \left[1 - w\left(f_{\mathrm{S}}\right)\right] \frac{C_0}{1-(1-k) f_{\mathrm{S}}} + w\left(f_{\mathrm{S}}\right)\left(C_0 - \frac{\Delta T}{m}\right) \tag{15}$$

This relation of C_{L} should be true for any binary alloys. But ΔT in Eq. (15) is also an unknown variable which makes the relationship between C_{L} and f_{S} implicit. According to the Lever rule and Scheil equation, the solid fraction could be expressed respectively as

$$f_{\mathrm{S}}^{\mathrm{Lever}} = \frac{\Delta T}{k\Delta T_0 + (1-k)\Delta T} \tag{16}$$

$$f_{\mathrm{S}}^{\mathrm{Scheil}} = 1 - \left(1 + \frac{\Delta T}{\Delta T_0}\frac{1-k}{k}\right)^{\frac{1}{k-1}} \tag{17}$$

where $\Delta T_0 = mC_0(1 - 1/k)$ is the solidification range. Interestingly, as shown in **Fig. 8**, the simulated solid fraction could be expressed as the mean of $f_{\mathrm{S}}^{\mathrm{Scheil}}$ and $f_{\mathrm{S}}^{\mathrm{Lever}}$, namely

$$f_{\mathrm{S}} = \frac{1}{2}\left(f_{\mathrm{S}}^{\mathrm{Lever}} + f_{\mathrm{S}}^{\mathrm{Scheil}}\right) = \frac{1}{2}\left[\frac{\Delta T}{(1-k)(\Delta T - mC_0)} + 1 - \left(1 - \frac{\Delta T}{mC_0}\right)^{\frac{1}{k-1}}\right] \tag{18}$$

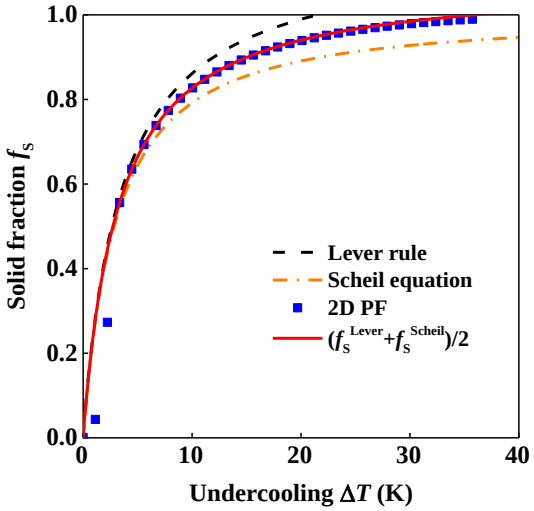

Fig. 8. Comparison of f_S predicted by two widely used microsegregation models (Lever rule and Scheil equation) and the 2D PF simulation of Al-1 wt.% Cu alloy at R_c = 0.1 K/s and N = 36.

Eq. (18) again arises from the fact that the Lever rule and the Scheil equation describe two limiting cases and the real non-equilibrium solidification is in between the predictions by these two simple models. Using Eq. (18), an explicit relationship between f_S and ΔT can be obtained naturally. However, the exact solution of Eq. (18) is difficult to be found because it is a high-order power equation. One way to solve the complicated Eq. (18) is to simplify it into a simple equation that can be solved easily. Here three intermediate variables are defined as

$$\begin{aligned} X &\equiv \frac{1}{1-\dfrac{\Delta T}{mC_0}} \\ p &\equiv \frac{1}{1-k} \\ q &\equiv 2f_S - 1 \end{aligned} \tag{19}$$

where X and q would be considered as the rescaled undercooling and solid fraction, respectively. Then Eq. (18) could be transformed into

$$q = -X^p - pX + p \tag{20}$$

with $0 < X < 1$ (for $k < 1$ and $m < 0$), $X > 1$ (for $k > 1$ and $m > 0$), and $-1 \le q \le 1$. It should be noticed that Eq. (20) is robust for different substitutional alloys with various k and m, because it is only a transformed from of Eq. (18) that depicts the relationship between the solid fraction and undercooling during solidification and no restriction of k and m is assumed in the derivation of Eq. (20). It is still quite difficult to solve Eq. (20) analytically, but as shown in **Fig. 9**, a linear approximation between q and X could be found for different k as

$$q = aX + b \tag{21}$$

with a and b being two fitting parameters. It is easily to found that when $X = 1$ ($\Delta T = 0$), $q = a + b = -1$, thus leading to that $b = -(a + 1)$. The values of the fitting parameter a for different k are given in **Fig. 10** and **Table. S1** in the Supplementary Materials. Since X and q are independent of k but Eq. (20) is equivalent to Eq. (21) which also relates to k, the parameter a must be a function of k. Indeed, from **Fig. 10**, a is proportional to $1/(k - 1)$ which reflects an inverse relationship to the solubility of solute in solid. A higher solubility means a smaller parameter a and thus a lower C_L. With a small solute partition coefficient ($k < 0.3$), an approximate linear relationship between a and k is found. For a larger k, the fitting parameter a could be obtained directly from **Fig. 10** and **Table. S1**, or by solving Eq. (20) numerically using Newton iteration method or other methods. Numerical practice shows that the Newton iteration method converges to the solution very fast after only a few iterations.

Combining the simplified linear Eq. (21) and the fitted parameter a in **Fig. 10** or **Table. S1**, an explicit relationship between C_L and f_S can be found readily. The variable X in Eq. (21) could be solved as

$$X = 1 + \frac{q+1}{a} \tag{22}$$

Replacing X in Eq. (19), the following equation could be obtained as

$$\Delta T = \frac{2 f_S}{a + 2 f_S} m C_0 \tag{23}$$

Then C_L in Eq. (15) could be expressed as a function of only three independent variables (C_0, f_S, and k) and an extra fitting parameter a (dependent on k), which is given as

$$C_L = C_0 \left[\frac{1 - w(f_S)}{1 - (1-k) f_S} + \frac{a}{a + 2 f_S} w(f_S) \right] \tag{24}$$

C_L predicted by Eq. (24) with $w(f_S) = f_S$ is plotted in **Fig. 11**(a), and a much better agreement with the simulation has been achieved, compared with the Lever rule and Scheil equation (as well as the Clyne-Kurz model and the Won-Thomas model considering the back diffusion), particularly at the late solidification stage with a high solid fraction. Moreover, it could be seen from **Fig. 11**(b) that the choice of the interpolation function $w(f_S)$ has no apparent influence on C_L predicted by Eq. (24), so it is reasonable to set a simple form of $w(f_S) = f_S$ as shown in **Fig. 11**(a). Therefore, the final analytical model of C_L is given as

$$C_L = C_0 \left[\frac{1 - f_S}{1 - (1-k) f_S} + \frac{a f_S}{a + 2 f_S} \right] \tag{25}$$

where the value of a is given in **Fig. 10** and **Table. S1** for k in the range of [0, 1) and (1, 10] which covers most binary alloy systems. As the concentration in solid can be obtained by $C_S = kC_L$, based on the definition of the solute segregation index, S_I also can be calculated accordingly as

$$S_{\mathrm{I}}=\left(\frac{C_{\mathrm{L}}}{C_0}-1\right)f_{\mathrm{L}}+\left(1-\frac{C_{\mathrm{S}}}{C_0}\right)f_{\mathrm{S}}\ (\text{for } k<1)$$
$$S_{\mathrm{I}}=\left(1-\frac{C_{\mathrm{L}}}{C_0}\right)f_{\mathrm{L}}+\left(\frac{C_{\mathrm{S}}}{C_0}-1\right)f_{\mathrm{S}}\ (\text{for } k>1) \tag{26}$$

with f_{L} the liquid fraction.

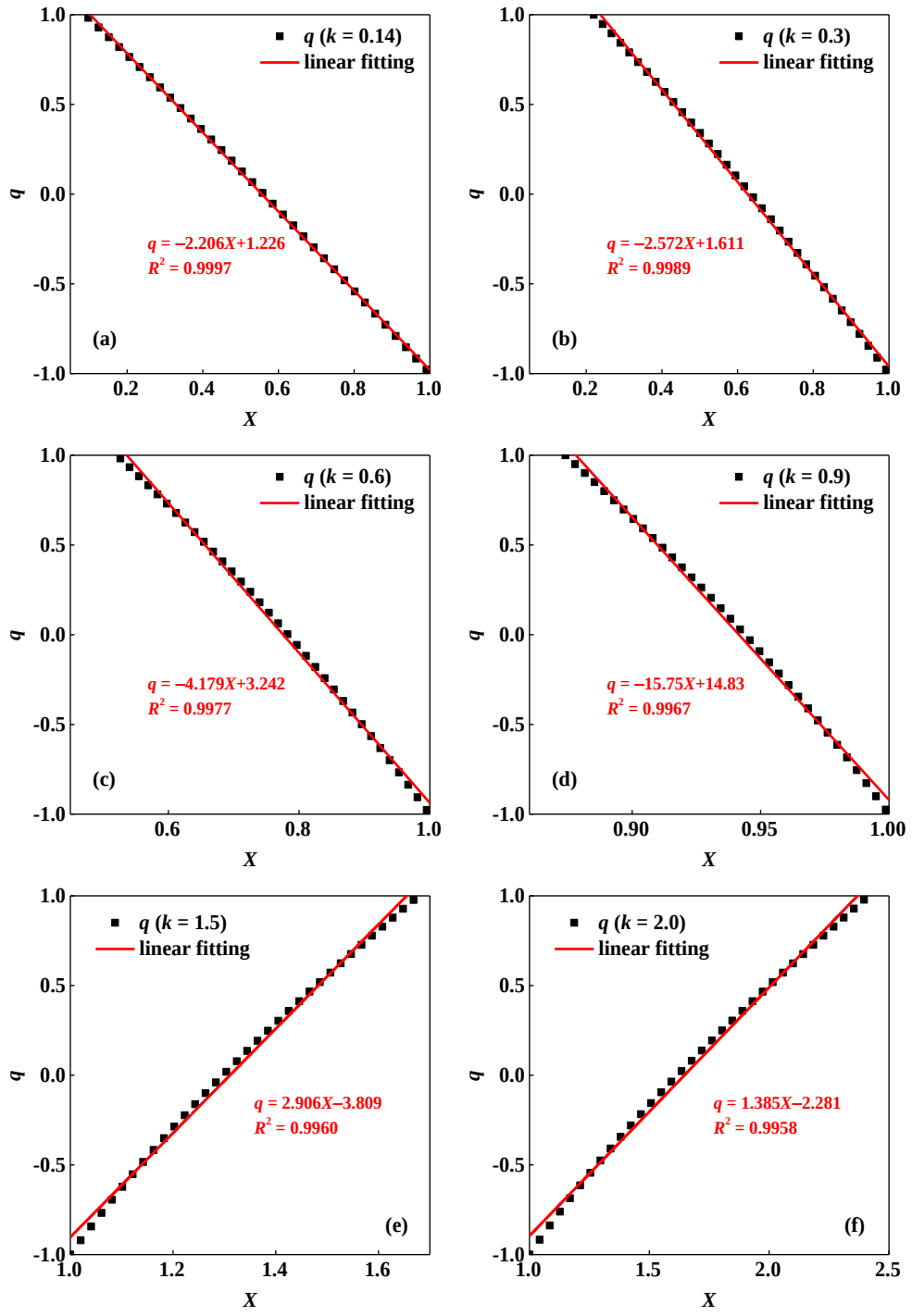

Fig. 9. Plotting of q against X with various solute partition coefficients. (**a**) $k = 0.14$ (for Al-Cu alloy); (**b**) $k = 0.3$; (**c**) $k = 0.6$; (**d**) $k = 0.9$; (**e**) $k = 1.5$; (**f**) $k = 2.0$.

The predicted S_I by Eq. (26) is plotted in **Fig. 12**, varying in the same manner as that in the PF simulation and showing a much better agreement with simulation than the Lever rule and Scheil equation before S_I reaches the peak value as $f_S < 0.73$. Accordingly, using Eqs. (25) and (26) one can easily calculate the solid fraction at which the microsegregation is most severe for a given binary alloy. The proposed microsegregation model is easily applied to a different alloy. Once the solute partition coefficient is known, the parameter a could be obtained through **Fig. 10** or **Table. S1**, and then C_L could be calculated directly by Eq. (25). However, it needs to be emphasized that the proposed model in the present work is still limited into the solidification where the local equilibrium at the solid-liquid interface is satisfied, which is consistent with the Scheil equation.

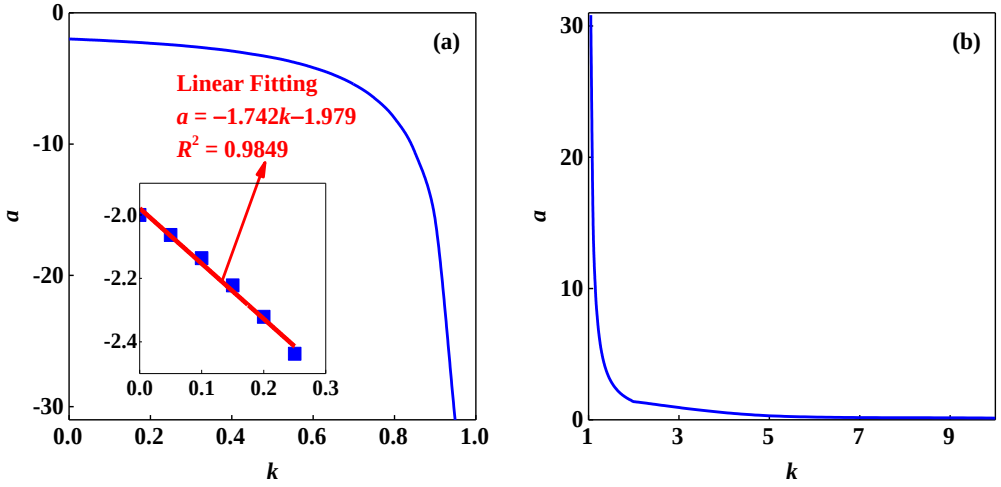

Fig. 10. Plotting of the fitting parameter, a, against k in Eq. (21). (**a**) $k < 1$; (**b**) $k > 1$. The inset figure in (a) shows the values of parameter a with $k < 0.3$, which could be well fitted by a linear function.

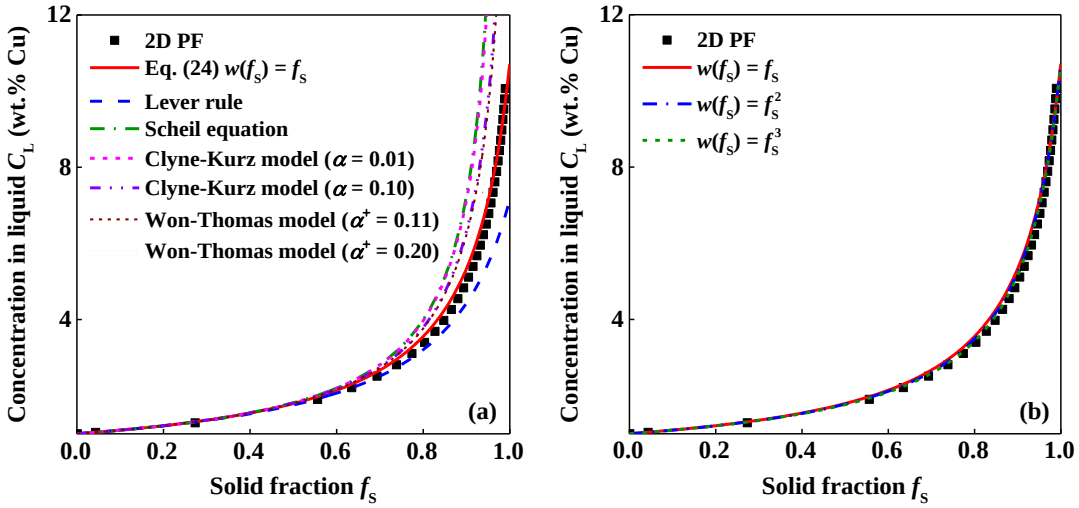

Fig. 11. (**a**) Comparison between C_L predicted by Eq. (24) and classical models, as well as the result in the 2D PF simulation with R_c = 0.1 K/s and N = 36. (**b**) C_L predicted by Eq. (24) with different choice of $w(f_S)$. SDAS in the simulation with R_c = 0.1 K/s and N = 36 is about 50~100 μm at f_S = 0.4~0.9, and for the other cases with N = 100~324, the average grain size is 150~500 μm. Therefore, the parameter $\alpha = 4D_S t_f/\lambda^2$ (as shown in **Table 1**), a constant related to SDAS or the grain size (in the case of globular grain with no developed sidebranches) in the Clyne-Kurz model is estimated to be 0.01~0.10. For the Won-Thomas model, the Fourier number is $\alpha^+ = \alpha + \alpha^C$ with α^C = 0.1 [11].

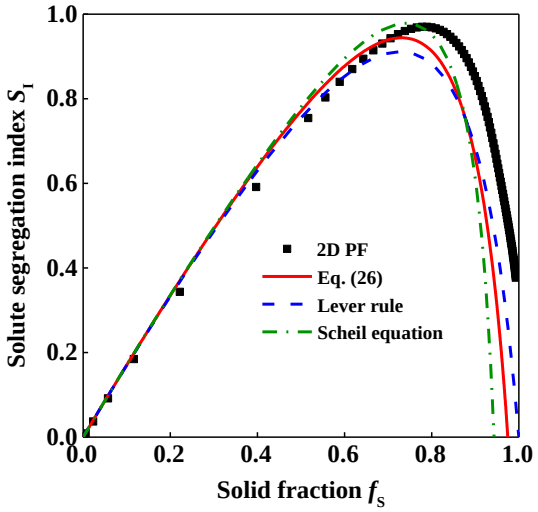

Fig. 12. Comparison of S_I in the 2D PF simulation at R_c = 0.1 K/s and N = 36 with predictions by Eq. (26) and the classical models (the Lever rule and Scheil equation).

5. Conclusions

Microsegregation behavior during polycrystalline equiaxed solidification of Al-Cu alloy is studied through quantitative phase-field simulations. With solidification proceeding, although more and more solute is rejected into melt and the average solute concentration in liquid increases gradually, the solute segregation index that reflects solute distribution homogeneity in both liquid and solid, evolves in an anomalous manner as first increasing to a certain peak value and then decreasing. Interestingly, the segregation index when liquid solidifies completely is almost the same for all cases, showing weak dependence on the grain refinement and cooling rate. This evolution behavior gives rise to the guidance of the best solid fraction for implementing rapid cooling or semisolid processing to reduce segregation. The grain size or morphology, and the cooling rate slightly influence the solute concentration in liquid, but they are not the crucial factors to change the microsegregation for the relatively slow solidification. For most of metallic alloys with substitutional solute elements, the effect of back diffusion on microsegregation is also not significant.

Moreover, it is revealed through PF simulations that the average solute concentration in liquid is between the Lever rule prediction and the maximum concentration in liquid that strongly relies on the applied undercooling. PF simulations also disclose that the solid fraction could be well estimated as the average of predictions by the Lever rule and Scheil equation with appropriate solute back diffusion in solid. Based on these findings, a new microsegregation model is deduced to accurately predict the solute concentration, particularly at the late solidification stage with a high solid fraction. The model is also as simple and easy-to-use as the Lever rule and Scheil equation, only relating to the sample nominal composition, solid fraction, partition coefficient, and a fitting parameter (also relying on the partition coefficient). The

segregation behavior and analytical model presented in this work would provide a new insight into the control of solute segregation in alloys during relatively slow solidification, and help to more accurately calculate phases and transformation kinetics of substitutional alloys by the CALPHAD method, as well as being in favor of simulations of macrosegregation in castings and ingots. For rapid solidification with solute trapping at the interface, same as the Lever rule or Scheil equation, the proposed model fails to predict the liquid concentration. Further improvement should be considered in the present model for the metallic alloys with interstitial solute elements which have large solute diffusion coefficients in solid. In these alloys, such as carbon steels, the back diffusion plays an important role in microsegregation.

Acknowledgement

This work was supported by the Science Challenge Project (Grant No. TZ2016004), the Youth Innovation Promotion Association CAS, the Youth Talent program of Shenyang National Laboratory for Materials Science (L2019F08), the Special Scientific Projects of Inner Mongolia, and French National Space Center (CNES), Convention N°174800/00.

References

[1] M. C. Schneider, C. Beckermann, A numerical study of the combined effects of microsegregation, mushy zone permeability and flow, caused by volume contraction and thermosolutal convection, on macrosegregation and eutectic formation in binary alloy solidification, Int. J. Heat Mass Transf. 38 (1995) 3455-3473.

[2] H. J. Thevik, A. Mo, The influence of micro-scale solute diffusion and dendrite coarsening upon surface macrosegregation, Int. J. Heat Mass Transf. 40 (1997) 2055-

2065.

[3] T. P. Battle, Mathematical-modeling of solute segregation in solidifying materials, Int. Mater. Rev. 37 (1992) 249-270.

[4] T. F. Bower, H. D. Brody, M. C. Flemings, Measurements of solute redistribution in dendritic solidification, Trans. Metall. Soc. AIME 236 (1966) 624-654.

[5] T. W. Clyne, W. Kurz, Solute redistribution during solidification with rapid solid-state diffusion, Metall. Trans. A 12 (1981) 965-971.

[6] I. Ohnaka, Mathematical-analysis of solute redistribution during solidification with diffusion in solid-phase, Trans. Iron Steel Inst. Japan 26 (1986) 1045-1051.

[7] T. P. Battle, R. D. Pehlke, Mathematical-modeling of microsegregation in binary metallic alloys, Metall. Trans. B 21 (1990) 357-375.

[8] V. R. Voller, A semi-analytical model of microsegregation in a binary alloy, J. Cryst. Growth 197 (1999) 325-332.

[9] V. R. Voller, A semi-analytical model of microsegregation and coarsening in a binary alloy, J. Cryst. Growth 197 (1999) 333-340.

[10] V. R. Voller, C. Beckermann, A unified model of microsegregation and coarsening, Metall. Mater. Trans. A-Phys. Metall. Mater. Sci. 30 (1999) 2183-2189.

[11] Y. M. Won, B. G. Thomas, Simple model of microsegregation during solidification of steels, Metall. Mater. Trans. A-Phys. Metall. Mater. Sci. 32 (2001) 1755-1767.

[12] D. M. Xu, A unified microscale parameter approach to solidification-transport process-based macrosegregation modeling for dendritic solidification: Part II. Numerical example computations, Metall. Mater. Trans. B-Proc. Metall. Mater. Proc. Sci. 33 (2002) 451-463.

[13] M. Ohno, M. Yamashita, K. Matsuura, Importance of microstructural evolution on prediction accuracy of microsegregation in Al-Cu and Fe-Mn alloys, Int. J. Heat Mass

Transf. 132 (2019) 1004-1017.

[14] A. M. Glenn, S. P. Russo, J. D. Gorman, P. J. K. Paterson, The effect of grain refining on the microsegregation of aluminium–magnesium alloy 5182, Micron 32 (2001) 841-850.

[15] D. Daloz, U. Hecht, J. Zollinger, H. Combeau, A. Hazotte, M. Založnik, Microsegregation, macrosegregation and related phase transformations in TiAl alloys, Intermetallics 19 (2011) 749-756.

[16] S. Y. He, C. J. Li, R. Guo, W. D. Xuan, Z. M. Ren, X. Li, Y. B. Zhong, Microsegregation Formation in Al-Cu Alloy under Action of Steady Magnetic Field, ISIJ Int. 58 (2018) 899-904.

[17] Y. J. Zhang, J. G. Li, Characterization of the Microstructure Evolution and Microsegregation in a Ni-Based Superalloy under Super-High Thermal Gradient Directional Solidification, Mater. Trans. 53 (2012) 1910-1914.

[18] D. Eskin, Q. Du, D. Ruvalcaba, L. Katgerman, Experimental study of structure formation in binary Al–Cu alloys at different cooling rates, Mater. Sci. Eng. A 405 (2005) 1-10.

[19] M. Paliwal, I.-H. Jung, The evolution of the growth morphology in Mg–Al alloys depending on the cooling rate during solidification, Acta Mater. 61 (2013) 4848-4860.

[20] M. C. Flemings, Behavior of metal alloys in the semisolid state, Metall. Trans. A 22 (1991) 957-981.

[21] C. A. Gandin, M. Rappaz, A 3D Cellular Automaton algorithm for the prediction of dendritic grain growth, Acta Mater. 45 (1997) 2187-2195.

[22] C. A. Gandin, J. L. Desbiolles, M. Rappaz, P. Thevoz, A three-dimensional cellular automaton-finite element model for the prediction of solidification grain structures, Metall. Mater. Trans. A-Phys. Metall. Mater. Sci. 30 (1999) 3153-3165.

[23] X. Zhang, J. Zhao, H. Jiang, M. Zhu, A three-dimensional cellular automaton model for dendritic growth in multi-component alloys, Acta Mater. 60 (2012) 2249-2257.

[24] A. Karma, Phase-field formulation for quantitative modeling of alloy solidification, Phys. Rev. Lett. 87 (2001) 115701.

[25] S. Y. Pan, M. F. Zhu, M. Rettenmayr, A phase-field study on the peritectic phase transition in Fe-C alloys, Acta Mater. 132 (2017) 565-575.

[26] S. Y. Pan, M. F. Zhu, Peritectic transformation with non-linear solute distribution in all three phases: Analytical solution, phase-field modeling and experiment comparison, Acta Mater. 146 (2018) 63-75.

[27] C. Beckermann, Modelling of future needs macrosegregation: applications and future needs, Int. Mater. Rev. 47 (2002) 243-261.

[28] M. H. Wu, A. Ludwig, A three-phase model for mixed columnar-equiaxed solidification, Metall. Mater. Trans. A-Phys. Metall. Mater. Sci. 37A (2006) 1613-1631.

[29] H. Combeau, M. Zaloznik, S. Hans, P. E. Richy, Prediction of Macrosegregation in Steel Ingots: Influence of the Motion and the Morphology of Equiaxed Grains, Metall. Mater. Trans. B-Proc. Metall. Mater. Proc. Sci. 40 (2009) 289-304.

[30] Y. F. Cao, Y. Chen, D. Z. Li, Formation mechanism of channel segregation in carbon steels by inclusion flotation: X-ray microtomography characterization and multi-phase flow modeling, Acta Mater. 107 (2016) 325-336.

[31] Thermo-Calc Software, 2013, TCFE, https://www.thermocalc.com/TCFE.htm (Last accessed 14 Jan 2015).

[32] B. Echebarria, R. Folch, A. Karma, M. Plapp, Quantitative phase-field model of alloy solidification, Phys. Rev. E 70 (2004) 061604.

[33] Y. Chen, A.-A. Bogno, N. M. Xiao, B. Billia, X. H. Kang, H. Nguyen-Thi, X. H.

Luo, D. Z. Li, Quantitatively comparing phase-field modeling with direct real time observation by synchrotron X-ray radiography of the initial transient during directional solidification of an Al–Cu alloy, Acta Mater. 60 (2012) 199-207.

[34] Y. Chen, B. Billia, D. Z. Li, H. Nguyen-Thi, N. M. Xiao, A. A. Bogno, Tip-splitting instability and transition to seaweed growth during alloy solidification in anisotropically preferred growth direction, Acta Mater. 66 (2014) 219-231.

[35] A. J. Clarke, D. Tourret, Y. Song, S. D. Imhoff, P. J. Gibbs, J. W. Gibbs, K. Fezzaa, A. Karma, Microstructure selection in thin-sample directional solidification of an Al-Cu alloy: In situ X-ray imaging and phase-field simulations, Acta Mater. 129 (2017) 203-216.

[36] A. K. Boukellal, J.-M. Debierre, G. Reinhart, H. Nguyen-Thi, Scaling laws governing the growth and interaction of equiaxed Al-Cu dendrites: A study combining experiments with phase-field simulations, Materialia 1 (2018) 62-69.

[37] K. Glasner, Nonlinear Preconditioning for Diffuse Interfaces, J. Comput. Phys. 174 (2001) 695-711.

[38] T. Z. Gong, Y. Chen, Y. F. Cao, X. H. Kang, D. Z. Li, Fast simulations of a large number of crystals growth in centimeter-scale during alloy solidification via nonlinearly preconditioned quantitative phase-field formula, Comput. Mater. Sci. 147 (2018) 338-352.

[39] Y. Chen, D. Z. Li, B. Billia, H. Nguyen-Thi, X. B. Qi, N. M. Xiao, Quantitative Phase-field Simulation of Dendritic Equiaxed Growth and Comparison with in Situ Observation on Al-4 wt.% Cu Alloy by Means of Synchrotron X-ray Radiography, ISIJ Int. 54 (2014) 445-451.

[40] W. Bangerth, D. Davydov, T. Heister, L. Heltai, G. Kanschat, M. Kronbichler, M. Maier, B. Turcksin, D. Wells, The deal.II Library, Version 8.4, J. Numer. Math. 24 (2016)

135-141.

[41] A. Bogno, H. Nguyen-Thi, G. Reinhart, B. Billia, J. Baruchel, Growth and interaction of dendritic equiaxed grains: In situ characterization by synchrotron X-ray radiography, Acta Mater. 61 (2013) 1303-1315.

[42] T. Z. Gong, Y. Chen, D. Z. Li, Y. F. Cao, P. X. Fu, Quantitative comparison of dendritic growth under forced flow between 2D and 3D phase-field simulation, Int. J. Heat Mass Transf. 135 (2019) 262-273.